

Chapter 1

Theoretical Motivation

1.1 The Standard Model of Particle Physics

The standard model of particle physics is based on a principle of symmetry under space-time and gauge transforms. The space-time symmetries are translations, rotations and lorentz boosts. Lorentzian symmetry is the statement that the scalar product

$$x^\mu y_\mu = \eta_{\mu\nu} x^\mu y^\nu \quad (1.1)$$

of two space-time vectors, x and y , is unchanged by transformations of the type

$$x^\mu \rightarrow x'^\mu = \Lambda^\mu_\nu x^\nu \quad (1.2)$$

where Λ^μ_ν is a rotation in 4 dimensions and $\eta_{\mu\nu}$ is the Minkowski metric. Since all of these space-time transforms can be considered as a change in a co-ordinate system, it is natural to assume that the laws of physics should be invariant under space-time transforms.

The standard model lagrangian is intended to describe the fundamental constituents of matter and their interactions with each other. The currently observed

particles are the fermions (six quarks and six leptons) and the photon, W/Z bosons and gluons that mediate the electromagnetic, weak and strong forces respectively. Experimentally, all of the fermions ¹ and the W and Z bosons are found to have mass, while the photon and gluons are massless. The electromagnetic force affects those particles with charge, the weak force violates parity and is seen to only affect left handed particles, and the strong force - mediated by gluons - affects only the quarks. The resultant theory must reflect all of these properties.

The standard model is constructed by building an interacting theory, and deal with the masses of particles later. The lagrangian density, \mathcal{L}_{dirac} , for massless spin 1/2 fields, $\Psi(x)$, is given by

$$\mathcal{L}_{dirac} = \bar{\Psi} (\gamma^\mu \partial_\mu) \Psi \quad (1.3)$$

where γ_μ are the Dirac matrices. The gauge boson interactions with the fermions are added by requiring that the lagrangian be invariant under transformations generated by the gauge group

$$SU(3)_C \times SU(2)_L \times U(1)_Y. \quad (1.4)$$

1.1.1 $U(1)_Y$ Gauge Symmetry

Taking $U(1)_Y$ transforms as an instructive example, one notices that the lagrangian is invariant under global phase transforms of the type

$$\Psi(x) \rightarrow e^{-i\omega Y(\Psi)} \Psi(x) \quad (1.5)$$

where the value of the hypercharge, Y , depends on the type of field. However, when the phase transform is a local, or gauge, transform ($\omega \rightarrow \omega(x)$) then the

¹The masses of the neutrino's are very small and only mass differences have been observed; as such they are set to zero in the Standard Model.

lagrangian is no longer invariant and has an additional piece

$$\Delta\mathcal{L} = -iY\partial_\mu\omega(x). \quad (1.6)$$

This is not an ideal solution because the phase transform is not a physical observable. It seems inappropriate then, that the physics at a particular point in space-time, depends on a the transform of every other point in space-time by the same amount.

It is possible to restore the symmetry of the lagrangian if the partial derivative, ∂_μ , is replaced with the covariant derivative D_μ ,

$$\partial_\mu \rightarrow D_\mu = \partial_\mu + ig'YB_\mu \quad (1.7)$$

and require that the vector field, B_μ , also undergoes a transform of the type

$$B_\mu \rightarrow B_\mu + \frac{1}{g'Y}\partial_\mu\omega(x). \quad (1.8)$$

Thus, to make the lagrangian invariant under gauge transforms, it is necessary to introduce a new field that is also affected by the phase transform. The upshot of all this, is that an interaction term has been introduced

$$\mathcal{L}_{int} = ig'Y\gamma^\mu\bar{\Psi}B_\mu\Psi \quad (1.9)$$

which tells us that the spinor field interacts with the vector gauge field B_μ with coupling strength, g' . It is then important to look for other terms involving B_μ that can be incorporated into the theory. The only other gauge invariant term that can be included in the lagrangian is the kinetic term

$$-\frac{1}{4}F_{\mu\nu}F^{\mu\nu} \quad (1.10)$$

where the field strength tensor, $F_{\mu\nu}$, is given by

$$F_{\mu\nu} = [D_\mu, D_\nu] = \partial_\mu B_\nu - \partial_\nu B_\mu. \quad (1.11)$$

Note that a mass term for the vector field, $\frac{m^2}{2}B_\mu B^\mu$, cannot be included as it is not invariant under the gauge transform given by equation 1.8. This holds for all the gauge transforms that are discussed here.

1.1.2 Non-Abelian symmetry and $SU(3)_C$

It is possible to include other interactions in the same way. The $U(1)_Y$ gauge transform is based on the spinor being transformed by a simple phase that is just a number at each point in space. However, there is no reason why, if the field contains some internal degrees of freedom, that the phase cannot be more complicated. Fields that are invariant under $SU(N)$ transforms have N internal degrees of freedom and transform as

$$\Psi(x) \rightarrow \Psi'(x) = e^{-i\omega^a(x)\mathbf{t}^a}\Psi(x) \quad (1.12)$$

where the \mathbf{t}^a are the $N^2 - 1$ generators of the group. These generators, \mathbf{t}^a , have a distinct algebra

$$[\mathbf{t}^a, \mathbf{t}^b] = if^{abc}\mathbf{t}^c \quad (1.13)$$

which leads to some new features in the lagrangian. The functions f^{abc} are the structure functions of the group. Each of the generators of $SU(N)$ can be represented in terms of an $N \times N$ matrix.

In the case of $SU(3)_C$, the quarks are assigned an internal degree of freedom known as colour. There are 8 generators (represented by the Gellman matrices) of the group and hence 8 gauge fields are required to keep the lagrangian symmetric under transformations. The covariant derivative - now a 3×3 matrix which acts on a three component field - is given by

$$\mathbf{D}_\mu = \partial_\mu \mathbf{I} + ig_s \mathbf{t}^a G_\mu^a \quad (1.14)$$

where \mathbf{I} is the unit matrix, g_s is the coupling strength and the gluon fields, $G_\mu^a(x)$, are the gauge fields required to keep the lagrangian invariant under the $SU(3)$ transform. The algebra of the $SU(N)$ generators leads to extra terms when the kinetic part of the lagrangian is evaluated for the gluons. These are the self-interactions given by

$$\mathcal{L}_{int} = g_s f^{abc} (\partial_\mu G_\nu^a) G_\mu^b G_\nu^c - \frac{1}{4} g_s^2 f^{abc} f^{ade} G_\mu^b G_\nu^c G_\mu^d G_\nu^e \quad (1.15)$$

which correspond to three and four-point gluon vertices.

There are a number of other properties of $SU(3)_C$ which require attention. These are asymptotic freedom and confinement, both of which can be explained by the running of the strong coupling, α_S , which is given by

$$\alpha_S = \frac{g_s^2}{4\pi}. \quad (1.16)$$

Consider the perturbative calculation of quark-quark scattering via gluon exchange. Such a calculation involves the evaluation of loop corrections to the gluon propagator, as shown in figure 1.1.2. The momenta of each line in the loop is not constrained and hence an integral over all possible momentum is required for the complete calculation. This, however, results in divergences in the calculation. The method for resolving this apparent problem is to recognise that the bare coupling, g_s , in the lagrangian is not the coupling that we observe experimentally. The divergences of the loop integral are absorbed into the strong coupling itself. This means that the coupling has been altered by the higher order corrections to the interaction, which in turn means that the coupling depends upon the momentum scale at which the interaction is evaluated.

In the case of the strong coupling, the renormalisation group equation is

$$\mu^2 \frac{\partial \alpha_S}{\partial \mu^2} = \beta(\alpha_S) \quad (1.17)$$

where μ is the momentum scale at which the ultraviolet subtractions of higher order terms are performed. The β function is calculable in perturbative QCD and is given by

$$\beta(\alpha_S) = -b\alpha_S^2 (1 + b'\alpha_S + b''\alpha_S^2 + \mathcal{O}(\alpha_S^3)) \quad (1.18)$$

where b , b' and b'' are the constants applicable to one, two and three loop corrections respectively. Using one loop as an example, the renormalisation equation can be solved by introducing a parameter, Λ , which indicates where the coupling becomes infinite. The running of the coupling is

$$\alpha_S(\mu^2) = \frac{1}{b \ln\left(\frac{\mu^2}{\Lambda^2}\right)}. \quad (1.19)$$

The sign of b is crucial as to how the coupling changes with scale. In QCD, b is calculated to be

$$b = \frac{1}{12\pi} (33 - 2n_f) \quad (1.20)$$

where the n_f is the number of active quark flavours in the calculation of fig 1.1.2(a). It is the self-interactions of the gluons that make b positive. As $Q^2 \rightarrow \Lambda^2$, the coupling diverges, which indicates that perturbative methods are not applicable at low momentum scales. However, at large momentum scales α_S decreases which tells us the theory is asymptotically free. The increase of the coupling as the momentum scale decreases means that objects are colour confined at large distances. This is the reason why all observed particles are in a colour singlet state.

1.1.3 $SU(2)_L$ Symmetry

The $SU(2)$ transformations follow the $SU(N)$ algebra. There are 3 generators, which can be represented by the Pauli matrices, and hence 3 gauge fields, $W_\mu^a(x)$,

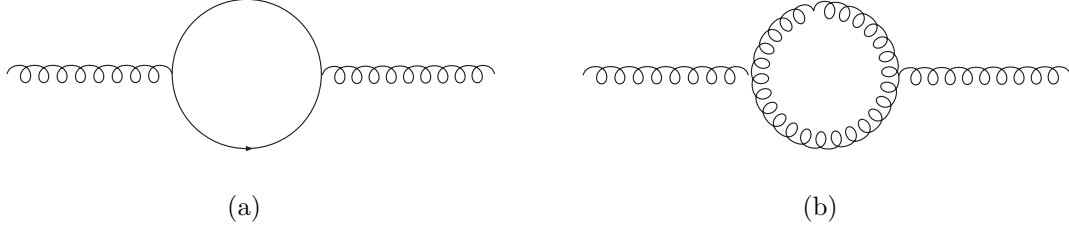


Figure 1.1: First order corrections to the gluon propagator, (a) shows a quark loop correction and (b) the gluon self interaction produces a gluon loop.

are required to keep the lagrangian invariant under the gauge transformation. The covariant derivative is now given by

$$\mathbf{D}_\mu = \frac{1}{\sqrt{2}} \left(\partial_\mu \mathbf{I} + i \frac{g}{2} \begin{pmatrix} W_\mu^3 & \sqrt{2} W_\mu^- \\ \sqrt{2} W_\mu^+ & -W_\mu^3 \end{pmatrix} \right) \quad (1.21)$$

with g being the coupling strength. The W^\pm are the bosons that mediate weak interactions such as muon decay and are given by

$$W^\pm = W_\mu^1 \pm i W_\mu^2. \quad (1.22)$$

The fermions are not assigned an new internal degree of freedom, but are firstly rewritten as the sum of a left-handed and right-handed component ($\Psi = \Psi_L + \Psi_R$), which can be obtained by the projection operators

$$P_{R,L} = \frac{1}{\sqrt{2}} (1 \pm \gamma^5). \quad (1.23)$$

The left handed fermions are then arranged into doublets which transform under $SU(2)_L$. The first generation of quark and lepton doublets, Q_u and L_e , are

$$Q_u = \begin{pmatrix} u_L \\ d_L \end{pmatrix} \quad L_e = \begin{pmatrix} \nu_{e,L} \\ e_L \end{pmatrix}. \quad (1.24)$$

The right-handed fermions are not assigned into doublets and hence do not transform under $SU(2)_L$. This is necessary because of the observed parity violations of the weak sector.

1.1.4 The Higgs Mechanism

The prescription so far has been to incorporate gauge boson interactions into the lagrangian by requiring symmetry under gauge transforms. However, this means that none of the gauge bosons can have an explicit mass term. Furthermore, mass terms for the fermions are forbidden because of the chiral nature of the lagrangian; a $m\bar{\Psi}\Psi$ term would mix the left and right-handed components of the field and hence would not remain invariant under the $SU(2)_L$ transform.

The mass problem is removed by the introduction of a complex scalar field, $\Phi_i(x)$, which transforms as a doublet under $SU(2)_L$ and has hypercharge $Y(\Phi) = \frac{1}{2}$. The lagrangian for this field is

$$\mathcal{L}_{scalar} = |\mathbf{D}_\mu \Phi|^2 - V(\Phi) \quad (1.25)$$

where the covariant derivative is one appropriate to $SU(2)_L$ and $U(1)_Y$. The potential, $V(\Phi)$, is

$$V(\Phi) = -\mu^2 \Phi_i^\dagger \Phi^i + \lambda (\Phi^\dagger \Phi)^2 \quad (1.26)$$

and the minimum of this potential occurs at $\Phi^\dagger \Phi = v^2 = \mu^2/2\lambda$. This means that the new scalar field has a non-zero vacuum expectation value. Furthermore, the vacuum is degenerate in $SU(2)_L$. The lagrangian is now no longer symmetric under transformations which simply moves us from one vacuum to a new one. The choice of true vacuum is said to spontaneously break the symmetry.

The field can be expanded about the expectation value and can be expressed, in the unitary gauge, as

$$\Phi = \begin{pmatrix} 0 \\ v + H \end{pmatrix} \quad (1.27)$$

where the higgs field, H , is observable and cannot be removed by a different choice of gauge. When the kinetic term is evaluated we obtain

$$|\mathbf{D}_\mu \Phi|^2 = \frac{1}{2} (\partial_\mu H)^2 + \frac{g^2 v^2}{2} W^{+, \mu} W_\mu^- + \frac{g^2 v^2}{2} \left(W_\mu^3 - \frac{g'}{g} B_\mu \right)^2 + int \quad (1.28)$$

where the interaction terms involve the Higgs field and the gauge bosons. The second term on the right of equation 1.28 gives a mass to the W bosons with $M_W = gv$. The third term is also a mass term but involves both the B_μ and W_μ^3 fields. This can be associated with the Z Boson, Z_μ , if the choice is made that

$$\begin{pmatrix} A_\mu \\ Z_\mu \end{pmatrix} = \begin{pmatrix} \cos \theta_W & \sin \theta_W \\ -\sin \theta_W & \cos \theta_W \end{pmatrix} \begin{pmatrix} B_\mu \\ W_\mu^3 \end{pmatrix} \quad (1.29)$$

where A_μ is the photon field and the weak mixing angle, θ_W is given by

$$g' = g \tan \theta_W. \quad (1.30)$$

Thus the gauge symmetry of $SU(2)_L \times U(1)_Y$ is broken down to a symmetry of $U(1)_{QED}$, and the weak force carriers have gained mass.

The presence of the scalar field doublet allows the introduction of new 'Yukawa' interaction terms in the lagrangian. These are interactions between the scalar field, right-handed and left-handed fermions. An example of such a Yukawa interaction is

$$\mathcal{L}_{Yukawa} = -G_e \bar{L}_L^i \Phi_i e_R + h.c. \quad (1.31)$$

where G_e is the Yukawa coupling. The Yukawa terms result in interactions term between the fermions and Higgs boson, but more importantly introduces a fermion mass term in the lagrangian. The Yukawa term of 1.31 results in a mass for the electron given by

$$\frac{G_e v}{\sqrt{2}} \bar{e} e. \quad (1.32)$$

Similar Yukawa terms can be introduced for any of the fermion fields. This provides a mechanism for introducing masses for all of the fermions despite the chiral nature of the standard model.

Chapter 2

Experimental Considerations

2.1 The Large Hadron Collider

The Large Hadron Collider (LHC) is a proton-proton collider based at CERN.

1. Acceleration of protons up to 14TeV (injectors main ring) magnet structure.
2. 4 interaction points
3. number of interactions.
4. Two running modes - low lumi high lumi - amount of data

2.2 The ATLAS Detector

The ATLAS detector, shown in figure 2.2, is a large, multi-purpose detector, designed with the ability to discover a variety of different physics signals during the lifetime of the LHC. To do this, the detector is comprised of a number of sub-detectors which fulfill a specific function. At the center of ATLAS, surrounding

the interaction point, is the inner detector (ID). The ID provides tracking, vertex reconstruction, transverse momentum measurement and some level of particle identification. Surrounding the ID are the electromagnetic and hadronic calorimeters, which provide energy and position measurement. On the outside of ATLAS is the muon spectrometer which provides muon tracking and momentum reconstruction.

The coordinate system used by the ATLAS detector defines the origin to be at the interaction point and the z direction to be along the beam line. Pseudo-rapidity, η is defined as

$$\eta = -\ln \tan \left(\frac{\theta}{2} \right) \quad (2.1)$$

where θ is the angle with respect to the z axis. The azimuthal angle, ϕ , in the transverse plane is defined to be zero in the x direction which points to the center of the LHC ring. Finally, there is a new length, used by detector elements covering the azimuthal direction, defined as $R_\phi = R\phi$ where R is the radial distance to the beam line.

2.2.1 The Inner Detector

The ID comprises 3 sub-detectors covering the pseudo-rapidity range $|\eta| < 2.5$. The detector nearest the beam is the pixel detector, which is surrounded by the semi-conductor tracker (SCT). The outermost detector is the transition radiation tracker (TRT). Each of these sub-detectors is split into 3 main components. One is a barrel region which is cylindrical about the beam line with the interaction point at the center. The other two are endcap regions, either side of the interaction point.

The pixel detector and the SCT are made from silicon. A charged particle passing through the silicon creates electron-hole pairs and a bias voltage across

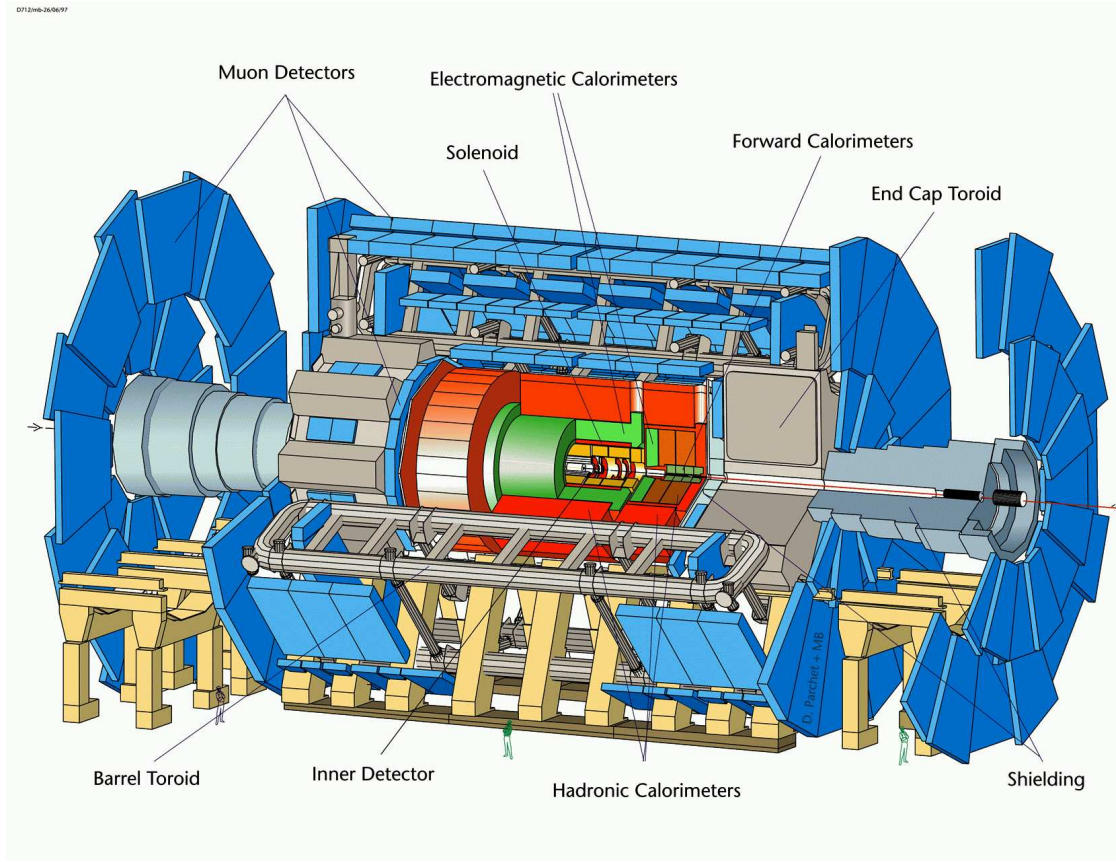


Figure 2.1: The ATLAS detector.

the silicon causes the charges to drift to a readout. If the amount of charge produced is greater than a threshold value then a particle hit is recorded.

The pixel detector is granular and segmented into pixels of $50\mu\text{m} \times 300\mu\text{m}$. A pixel module consists of 61440 pixels in a $21.4\text{mm} \times 62.4\text{mm}$ rectangle. In the barrel region, the longer edge of each module is aligned in the z direction and the shorter edge in R_ϕ . The barrel consists of 3 layers of modules, with each layer providing coverage of $|\eta| < 1.7$ and complete coverage in azimuth. The granularity of the pixels allows precise measurements in R_ϕ and z , with a resolution of $12\mu\text{m}$ and $66\mu\text{m}$ respectively. Each pixel end-cap consist of 5 disks of modules covering the

pseudo rapidity range $1.7 < |\eta| < 2.5$. The position resolution is $12\mu\text{m}$ in R_ϕ and $77\mu\text{m}$ in R .

The SCT is made of single sided p-on-n silicon microstrip detectors which are $6.36 \times 6.40\text{cm}$. Each detector consists of 768 strips of $80\mu\text{m}$ pitch. A module consists of 4 of these detectors, which are wire bonded in pairs to give a length of 12.8cm . These pairs are then glued back to back at a crossing angle of 40mrad . This allows precision measurement in one direction, using the granularity provided by the microstrip width, and another measurement to be made using small angle stereo. In the barrel ($|\eta| < 1.4$), there are 4 layers of modules which are arranged so that the strips offer segmentation of the R_ϕ direction. This results in a resolution in R_ϕ to be $16\mu\text{m}$ and the small angle stereo gives a z measurement accurate to $580\mu\text{m}$.

The two SCT end-caps each consist of 9 disks covering the range $1.4 < |\eta| < 2.5$. The end-cap modules are constructed in the same way as the barrel modules. However, the microstrips themselves are tapered. The modules are aligned on the disks so that one set of strips is in the radial direction, again giving precision measurements in the R_ϕ direction. The resolution of the end-cap measurements in (R_ϕ, R) is the same as the barrel measurements in (R_ϕ, z) .

The TRT is based on straw detector technology. The straws are filled with gas, and a charged particle traversing the gas causes ionisation. The electrons drift toward a wire readout in the centre of the straw, due to a bias voltage. A particle hit is defined in a similar way to the silicon detectors using a threshold of collected charge. The TRT is made of straws 4mm in diameter and 144cm long which are divided into two parts to reduce occupancy. The barrel section ($|\eta| < 0.7$) has 50000 straws, aligned lengthways in the z direction. The end-cap

wheels have 320000 radial straws arranged in 18 wheels per end-cap, covering the region $0.7 < |\eta| < 2.5$. Drift time measurements result in a resolution of $170\mu\text{m}$ per straw. A charged particle passing through the TRT gives typically 36 hits per track.

Radiator material is placed between the straws. Particles with $\beta\gamma \geq 1000$ will emit transition radiation photons at the radiator-straw boundary. The emitted radiation is absorbed by Xenon and results in more ionisation than just the initial particle alone. The TRT uses a second, higher threshold to determine whether the hit consists of a particle plus transition radiation. This mechanism allows electron-pion separation in the transverse momentum range $10 < p_T < 100\text{GeV}$ with approximately 90% efficiency.

The ID is surrounded by a superconducting central solenoid (CS) magnet which provides a 2T magnetic field in the z direction. The CS is kept at 4.5K and shares the same vacuum vessel as the electromagnetic barrel calorimeter. The charged particles bend in the presence of the magnetic field and the p_T of the particle can be obtained from the radius of curvature of the track. The large number of track hits in the TRT, coupled with the precision measurements of the silicon detectors, result in excellent reconstruction of particle pseudo-rapidity, azimuth, impact parameter, d_0 , and vertex identification, z_0 . The resolution of reconstructed muon track parameters are []:

$$\begin{aligned}\sigma\left(\frac{1}{p_T}\right) &= 0.36 + \frac{13}{p_T \sin \theta} \quad (TeV^{-1}) & \sigma(\phi) &= 0.075 + \frac{1.8}{p_T \sin \theta} \quad (mrad) \\ \sigma(\cot \theta) &= \left(0.7 + \frac{2.0}{p_T \sin \theta}\right) \times 10^{-3} & \sigma(d_0) &= 11 + \frac{73}{p_T \sin \theta} \quad (\mu m) \\ \sigma(z_0) &= 87 + \frac{115}{p_T \sin \theta} \quad (\mu m).\end{aligned}\tag{2.2}$$

Pions and electrons are less well measured. Pions have a probability of undergoing a nuclear interaction which causes tails in reconstructed track parameters. This problem is removed by the standard track quality cuts which are at least 9 precision hits (out of 11), more than 2 pixel hits and a transverse impact parameter $< 1\text{mm}$. The effect of track quality requirements reduces the efficiency of π track reconstruction but leads to similar resolutions as equation 2.2. Electrons on the other hand emit brehmstrahlung radiation which leads to a broadening of the smeared distributions of $1/p_T$, d_0 and ϕ .

2.2.2 The Calorimeters

Calorimeters measure the total energy of particles by complete absorbtion. The two ATLAS calorimeters use alternating sheets of material to repeatedly sample the energy. The first type of material causes the particles to shower into a number of secondary particles. The second type of material absorbs some of the energy of the produced particles. This process is repeated in many layers until all of the energy is absorbed.

The electromagnetic calorimeter uses a lead/liquid argon combination to measure the energy of photons and electrons. In the presence of heavy nuclei, electrons emit bremsstrahlung radiation. Photons on the other hand split into an electron-positron pair. Thus an incident electron or photon will result in a shower of new particles when passing through the lead layer. The electrons produced in the shower cause ionisation in the liquid argon and the charge is collected on copper electrodes.

The barrel EM calorimeter covers the region $|\eta| < 1.475$ and the end-caps cover $1.375 < |\eta| < 3.2$. However, in the pseudo-rapidity region $|\eta| < 1.8$, the EM

calorimeter is preceded by a presampler which is a just a layer of liquid argon. The reason is that the material preceeding the calorimeter, especially the solenoid, can cause showering. Hence, the presampler corrects for this energy loss.

The EM barrel calorimeter is split into 3 sampling regions of differing granularity. The inner sampling layer has a granularity of 0.003×0.098 in $\eta \times \phi$ and a depth of 4.3 radiation lengths. The second layer absorbs the majority of the energy of the particle due to a radial depth of 16 radiation lengths. The granularity of the second sampler is 0.0245 in both η and ϕ . The final layer is coarser, with a granularity of 0.0245×0.049 in $\eta \times \phi$, and has a depth of 2 radiation lengths. The EM end-caps have a more complicated geometry, shown in table 2.1, where the granularity and number of samplings depends on the pseudo-rapidity.

The energy resolution, σ_E , of the EM calorimeter is parameterised by

$$\frac{\sigma_E}{E} = \sqrt{\left(\frac{a^2}{E} + b^2\right)} \quad (2.3)$$

where E is the energy of the particle, a^2 is a sampling term ($\%GeV^{1/2}$) and b^2 is a constant (%). The sampling term varies between 8 and 12 from low to high rapidity. The constant term is less than 0.5% for electrons and less than 0.25% for photons.

The hadronic calorimeters are used to measure the energy of the baryons and mesons. In the barrel ($|\eta| < 1.0$) and extended barrel ($0.8 < \eta < 1.7$) regions, iron is used to shower the hadrons and 3mm scintillating tiles are used as the absorber. Each side of the tile is read out by a photomultiplier tube (PMT). The readout cells are divided to give 64 modules in azimuth. In the z direction, the readout from the cells are grouped in such a way so that the resulting granularity is 0.1×0.1 in $\eta \times \phi$ for the first 2 samplings. The final sampling is less granular with $\eta = 0.2 \times 0.1$.

End-Cap	Sampling number	$ \eta $	$\eta \times \phi$
EM	1	$1.375 < \eta < 1.5$	0.025×0.1
		$1.5 < \eta < 1.8$	0.003×0.1
		$1.8 < \eta < 2.0$	0.004×0.1
		$2.0 < \eta < 2.5$	0.006×0.1
		$2.5 < \eta < 3.2$	0.1×0.1
	2	$1.375 < \eta < 2.5$	0.025×0.025
		$2.5 < \eta < 3.2$	0.1×0.1
	3	$1.5 < \eta < 2.5$	0.05×0.025
HEC	All	$1.5 < \eta < 2.5$	0.1×0.1
	All	$2.5 < \eta < 3.2$	0.2×0.2

Table 2.1: The granularity ($\eta \times \phi$) of the end-cap calorimeters.

The hadronic end-cap (HEC), $1.7 < \eta < 3.2$, uses copper to provide the hadron shower and an 8.5mm liquid argon gap as the absorber. The end-cap system is split into 2 wheels. There are 4 sets of samplings, but the granularity depends on the pseudo-rapidity as in the EM end-cap. The granularity is given in table 2.1. The forward calorimeter, $3.1 < \eta < 4.9$, also uses liquid argon. However, the LAr gap is only $250\mu\text{m}$ throughout the structure. This is achieved by using a tungsten matrix with regularly spaced channels. Cylindrical rods are placed in the channels and carry high voltage, which causes the charge drift in the LAr gap. The resulting granularity is $\eta \times \phi = 0.2 \times 0.2$.

The resolution in energy measurement for hadrons takes into account energy deposited in the EM calorimeter, the hadronic calorimeter and dead material in the detector. The resolution is also parameterised using equation 2.3. The corre-

sponding sampling and constant terms for pions obtained from test beam data [] are given in table 2.2

$ \eta $	a^2 ($\%GeV^{0.5}$)	b^2 (%)
0.3	40 ± 1	3.0 ± 0.1
1.3	44 ± 3	1.6 ± 0.3
$1.8 < \eta < 3.05$	$55 < a^2 < 60$	$2.5 < b^2 < 3.0$

Table 2.2: The sampling (a^2) and constant (b^2) terms for hadrons. The final resolution combines information from the EM and hadronic calorimeters and corrects for energy lost in dead material such as the cryostat wall.

2.2.3 The Muon Spectrometer

The muon spectrometer measures is designed to measure the transverse momentum of muons by measuring the radius of curvature of muon track in a magnetic field. The magnetic field is provided by three superconducting air-core toroid systems (shown in figure 2.2). The end-cap toroids (ECT) are inserted into the barrel toroid (BT). The overall bending power is 2-6 Tm in the pseudo-rapidity range $|\eta| < 1.3$ and 4-8 Tm in the region $1.6 < |\eta| < 2.7$. The overlap region of the BT and ECT, $1.3 < |\eta| < 1.6$, has a lower bending power.

The muon spectrometer is divided into precision and trigger chambers. In the barrel region, $|\eta| < 1.0$, the precision chambers are 3 stations of monitored drift tubes (MDT's). The MDT's are made from 30mm aluminium tubes, with a $50\mu\text{m}$ W-Re readout wire in the centre. The single wire resolution is $80\mu\text{m}$. A super-layer is defined as 3 layers of tubes in the inner station and 4 layers in middle and outer stations. The chambers themselves consist of 2 super-layers, one on each side of

the support structure to which they are attached. The barrel muon spectrometer consists of 1194 such chambers.

In the end-caps, the precision chambers are MDT's in the region $1.0 < |\eta| < 2.0$ and cathode strip chambers (CSC's) in the region $2.0 < |\eta| < 2.7$. The CSC's are multi-wire proportional chambers with the first set of cathode strips perpendicular to the anode. The precision point is measured by reading out the induced charge on the cathode due electron avalanche on the anode. The second set of cathode strips are parallel to the anode and thus provide the transverse component. The position resolution of the cathode strips is expected to be approximately $60\mu\text{m}$.

The momentum resolution of the muon spectrometer depends on the transverse momentum and pseudo-rapidity of the muon itself. High p_T muons are bent less in the magnetic field and hence the radius of curvature is less well measured. In the overlap region between barrel and end-cap toroids, the bending power is smaller and hence the momentum less well measured. Even so, the momentum resolution of the muon spectrometers is approximately 3% for muons with $p_T = 30 - 100\text{GeV}$, better than 5% for $p_T < 300\text{GeV}$ and approximately 10% for 1TeV muons.

The trigger chambers are resistive plate chambers (RPC's) in the barrel region, $|\eta| < 1.0$, and thin gap chambers (TGC's) in the region $1.0 < |\eta| < 2.4$. An RPC unit is made of 2 parallel plate resistive plates separated by a gas gap. Ionised electrons are multiplied by an electric field of 4.5kV mm^{-1} . The charge is read out by perpendicular sets of metal strips on either side of the unit. The η strips are aligned with the wires in the MDT's. The ϕ strips are then used in offline reconstruction. The resolution in space-time of the RPC's is approximately $1\text{cm} \times 1\text{ns}$. Each trigger chamber consists of 2 such units. The TGC's are essentially multi-wire proportional chambers. The gas gap is 2.8mm and the wire pitch is

1.8mm. The wires are aligned with the wires in the MDT's. Graphite cathode read-out strips are arranged perpendicular to the anode wires and provide the second coordinate in offline reconstruction.

2.2.4 Trigger and Data Acquisition

It is not desirable for the ATLAS collaboration to store all the event data from every bunch crossing. Firstly, each event will occupy approximately 1MB of memory in offline storage. As the bunch crossing rate at the LHC is 40MHz, this would correspond to a data rate of 40TB s⁻¹. Secondly, the majority of these events are soft QCD events. New physics signals, such as the discovery of the Higgs boson, are relatively rare and searching through such a large data set for a potential signal would take too long. It is better therefore, to examine the data immediately and store the event permanently if it passes a set of criteria. This is known as triggering.

The ATLAS trigger is performed in 3 successive stages; level 1, level 2 and the event filter. The information from each sub-detector is pushed into pipeline memories. Each sub-detector then can identify which memory block corresponded to a particular bunch crossing. For practical and economical reasons the length of the pipelines must be kept short which limits the time the sub-detector will retain the information.

The level 1 trigger has the initial responsibility of retaining events of possible interest. The decision to keep an event must be made within 2.5 μ s otherwise the relevant information from some sub-detectors will be lost. The trigger relies on reduced granularity information from the muon spectrometer and calorimeters in order to define objects of interest. Muons are identified using just the RPC's and

Trigger	Rate (kHz)
MU6	23
EM20I	11
EM15I $\times 2$	2
J180	0.2
J75 $\times 3$	0.2
J55 $\times 4$	0.2
J50 + XE50	0.4
T20 + XE30	2
Other	5

Table 2.3: Low luminosity level 1 trigger menu. The following codes are standard in level 1: MU(muon spectrometer), EM(electromagnetic calorimeter), J(jet), T(tau), XE(missing E_T) and I is an isolation criterion. For example EM20I means the 2×2 EM tower object must have an $E_T > 20$ and be isolated from other EM activity.

TGC's. The calorimeter trigger works on tower blocks of 4×4 and used to define electron/photon, tau, jet, missing E_T and scalar E_T objects.

A physics menu provides a list of criteria that define objects of potential interest. The level 1 physics menu is shown in table 2.3. The jet triggers are very high in E_T because of the very large QCD rate at low E_T . The muon p_T requirement is low in order to keep soft muons from B-physics events. If an object passes one of these criteria, the entire event is kept. The data is then read out, formatted and stored in read-out buffers (RoB's). The final data rate of events selected at level 1 is 75kHz.

The level 2 trigger operates on regions-of-interest (RoI's). An RoI is a small

amount of information provided by level 1 on each object that passes a level 1 trigger. Level 2 starts out by confirming the level 1 result. The level 2 trigger then refines the result by searching other sub-detectors for relevant information. In the case of muons for example, an isolation criterion can be applied by looking for activity in the calorimeters. Level 2 then defines global trigger objects based on information from all sub-detector and makes a decision to keep the event or not. The total processing time at level 2 is approximately 10ms and the data rate which is passed to the event filter is 1kHz.

2.3 The FP420 Project

FP420 is a proposed new sub-detector capable of measuring the momenta of protons scattered in central exclusive processes.

Chapter 3

Analysis

3.1 Jet Algorithms

Final states containing coloured partons undergo parton showering and hadronisation as outlined in section ???. This means that the observable final state will consist of collimated streams of hadrons, which are called jets. Naively, one would expect a di-parton system to result in a 2 jet final state. However, hard, wide-angle radiation in the parton showering stage will produce a new stream of particles and could look like a 3 jet system. The exact classification of a system in terms of the number of jets depends on the jet algorithm used. In this section, the mid-point cone and K_T clustering jet algorithms are reviewed.

The ideal jet algorithm, as defined by a Tevatron Run II Jet Physics working group ??, should possess the following criteria:

1. The algorithm should be fully defined.
2. The algorithm should be collinear and infrared safe.
3. It should perform equally well at parton, hadron and detector level.

4. It should not depend on detector quantities such as cell/tower size.

The last two criteria will only ever be approximately true in a real algorithm due to detector resolution and granularity. The size of the towers and cells will not allow the direction of the particle to ever be exactly known, hence the algorithm will perform slightly differently at detector level. The first criterion is a requirement of the algorithm definition. The second criterion is required so that not only is the perturbative QCD calculation free of soft and collinear singularities, but the result after jet-finding is insensitive to soft or collinear radiation.

3.1.1 The Mid-Point Cone Algorithm

The mid-point cone algorithm has a geometrical motivation and defines a jet to be a group of particles within a cone of radius, R_{cone} , in $\eta \times \phi$ space. The cone radius is used to define the spatial extent of the jet. The basic cone algorithm, as used in Run I at the Tevatron, works as follows:

1. A seed is assigned to every particle or calorimeter tower. This seed is used as the centroid direction, (η^C, ϕ^C) , for a proto-jet.
2. All particles, i , that are satisfy the requirement

$$(\eta^i - \eta^C)^2 + (\phi^i - \phi^C)^2 \leq R_{cone}^2 \quad (3.1)$$

are then clustered to find the proto-jet. The axis of the proto-jet, (η^J, ϕ^J) , is found by the E_T weighted sum of particles in the jet, i.e

$$\eta^J = \frac{\sum E_T^i \eta^i}{\sum E_T^i} \quad \phi^J = \frac{\sum E_T^i \phi^i}{\sum E_T^i} \quad (3.2)$$

where the sum is over all particles within the cone, C .

3. The proto-jet axis is then used as the seed for a new cone and step 2 repeated.
In this way, the calculation is iterated to find stable proto-jets when $\eta^C = \eta^J$ and $\phi^C = \phi^J$.
4. Steps 2 and 3 are repeated to find all possible proto-jets.
5. The above procedure will produce jets which overlap in $\eta \times \phi$ space. The lower E_T jet is discarded if the fraction, f , of its energy that is shared with the other jet is greater than an overlap fraction, O . If $f < O$ then the particles in the overlap region are assigned to the nearest jet centre.

This algorithm would not be infra-red safe as it stands. Figure 3.1 highlights the problem of soft radiation in the middle of 2 possible proto-jets which are separated by more than R_{cone} in $\eta \times \phi$ space, but less than $2R_{cone}$. It is clear that the number of jets in the final state is dependent on whether soft radiation is emitted between the jets. In the absence of the soft radiation, 2 jets will be found. However, the soft radiation between the jets would provide a new seed and now only 1 jet will be found. Hence the final result is sensitive to soft radiation between the jets.

This problem is removed if, in addition to using the particles as seeds, a seed is created in the middle (in $\eta \times \phi$) of every two particles that are separated by less than $2R_{cone}$. Now the final result is independent of soft radiation like that in figure 3.1. This type of algorithm is called a mid-point cone algorithm.

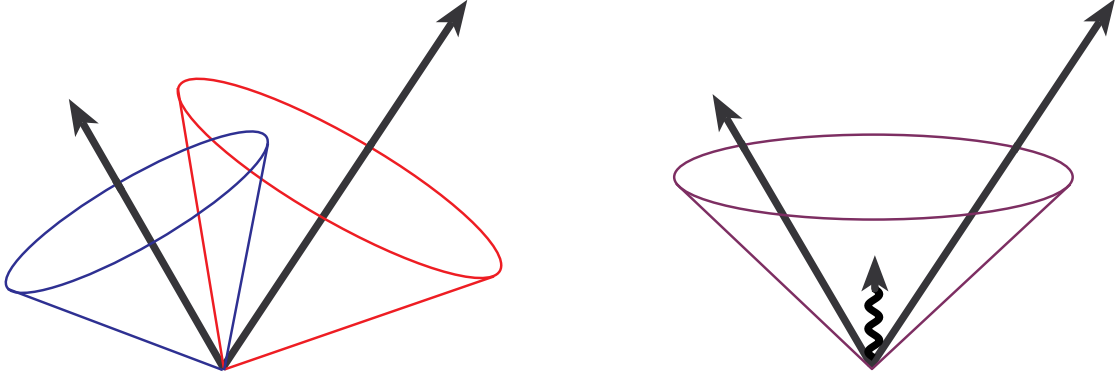


Figure 3.1: Infra-red sensitivity of a basic cone algorithm. The two hard partons, represented as arrows, are separated by more than R_{cone} but less than $2R_{cone}$. In the absence of radiation between the jets (left), 2 distinct jets will be found. However, radiation between the jets (right) would cause only 1 jet to be found.

3.1.2 The K_T Clustering Algorithm

The K_T algorithm is kinematically motivated. The prescription is to merge particles together if they have a low transverse momentum with respect to one another. The basic inclusive K_T algorithm, outlined in [?], defines jets in the following way:

1. The resolution variables d_{kB} and d_{kl}

$$d_{kB} = d_{kl} = \quad (3.3)$$

are computed for every object, k , and every pair of objects, k l . At the start of the algorithm, the list of objects are particles or calorimeter towers.

2. The d_{kB} are scaled by a user defined parameter, R_{K_T} ,

$$d_k = R_{K_T}^2 d_{kB} \quad (3.4)$$

3. The smallest resolution variable is found in the set of d_k and d_{kl} . If this is a d_{kl} , then objects k and l are merged into a single object. If a d_k is the

smallest resolution variable then k is defined as a jet and removed from the list .

4. Steps 1 - 3 are repeated until all objects are defined as jets.

This algorithm is insensitive to soft or collinear radiation. It is the nature of the K_T algorithm to merge soft/collinear particles first because these have the smallest resolution variable d_{kl} .

3.2 Central Exclusive Jet Variables

3.3 Central Exclusive $H \rightarrow b\bar{b}$ at ATLAS

The aim of this section is to determine whether it is possible to see the $H \rightarrow b\bar{b}$ channel in central exclusive production at ATLAS. The choice of jet algorithm will affect the reconstructed exclusive variables and hence the choice of cut required to remove the background. The strategy below is to firstly extract the best kinematic matching cuts for each jet algorithm and determine whether a particular algorithm performs better than the others. Further possible exclusivity requirements are then examined in order to reduce the non-exclusive backgrounds further. Finally, the cross section for exclusive $H \rightarrow b\bar{b}$ is given, along with the impact of current experimental triggers.

3.3.1 Backgrounds

The backgrounds to the central exclusive $H \rightarrow b\bar{b}$ channel are divided into 3 categories; central exclusive, double pomeron exchange and pile-up. The central exclusive backgrounds are $b\bar{b}$ and gg production and are produced, along with

the Higgs signal, using the ExHuME Monte Carlo. The $b\bar{b}$ background will have identical kinematic matching properties to the signal and so cannot be reduced from information from FP420. However, equation ?? shows that the exclusive di-quark background is, at a given central mass, strongly peaked in the large pseudo-rapidity region. Hence an E_T and η cut will reduce this background. The gg background can be reduced in a similar way.

The double pomeron exchange processes were simulated using the POMWIG Monte Carlo. There are 3 processes that act as background - Higgs, $b\bar{b}$ and jj where the j are light quark or gluon jets. These backgrounds have 2 intact protons in the final state and a jet-like central system. However, the kinematics of the 2-jet event measured in the ATLAS detector should not match the kinematics measured in FP420 because of the presence of pomeron remnants in the final state. Section 3.3.2 deals with the correct identification of these events.

The pile-up background involves 2 single diffractive (SD) overlap events plus a QCD event at the LHC. The QCD events are again $b\bar{b}$ and jj . However, the protons from the SD overlap events have absolutely no relation to the QCD event and as such, one would expect the kinematics to very rarely match between FP420 and the central ATLAS detector. Furthermore, the protons that gave rise to the QCD event have broken up and this deposits extra energy in the central detector and leaves extra tracks in the central detector. This type of background estimated in section 3.3.3.

3.3.2 Jet Algorithm effects and Kinematic Matching Cuts

Starting with just the $H \rightarrow b\bar{b}$ events, the 3 types of jet algorithm were applied. Event were only retained if the highest transverse energy jet had $E_T > 40\text{GeV}$. The

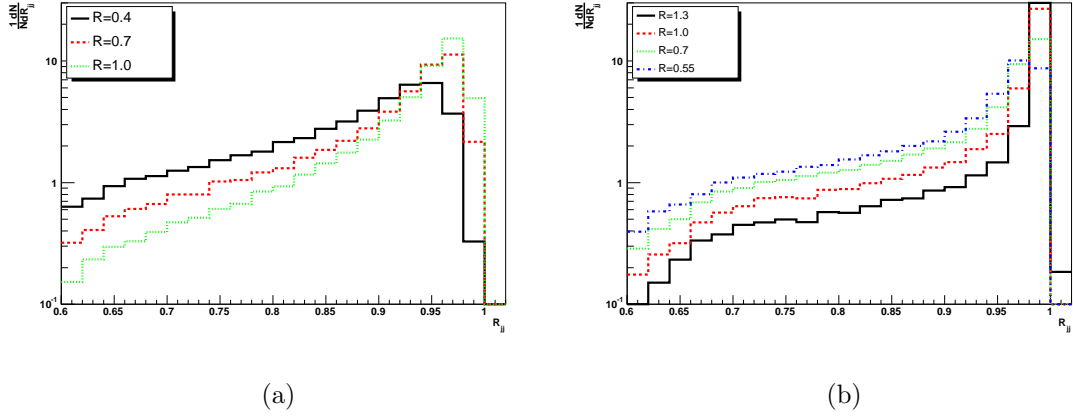


Figure 3.2: The reconstructed R_{jj} distribution using the cone (a) and inclusive K_T (b) jet-finding algorithms. The effect of changing R_{cone} or R_{K_T} is also shown.

effects of the cone and inclusive K_T algorithm on the reconstructed R_{jj} distribution are shown in figure 3.2. The R_{jj} distribution has a peak close to 1.0 but a long tail to medium R_{jj} values. This is due to hard final state radiation from one of the b quarks not being recovered by the jet algorithm. The effect of reducing the cone radius results in less of the energy being reconstructed in the 2-jet system and a flatter R_{jj} distribution as expected. Reducing the K_T R parameter has a similar effect.

In contrast, the variable R_j is defined to be not as affected by very hard radiation from one of the jets. The R_j distribution shown in figure 3.3 is a narrower peak than the R_{jj} distribution with the long tail removed. Furthermore, changing the cone radius, or inclusive K_T R -parameter, has less effect on the distribution. This makes R_j a robust variable for defining exclusive events. The inclusive K_T algorithm performs slightly better than the cone algorithm because the distribution is less susceptible to changes in the R_{K_T} . Both algorithms produce similar shapes of distribution.

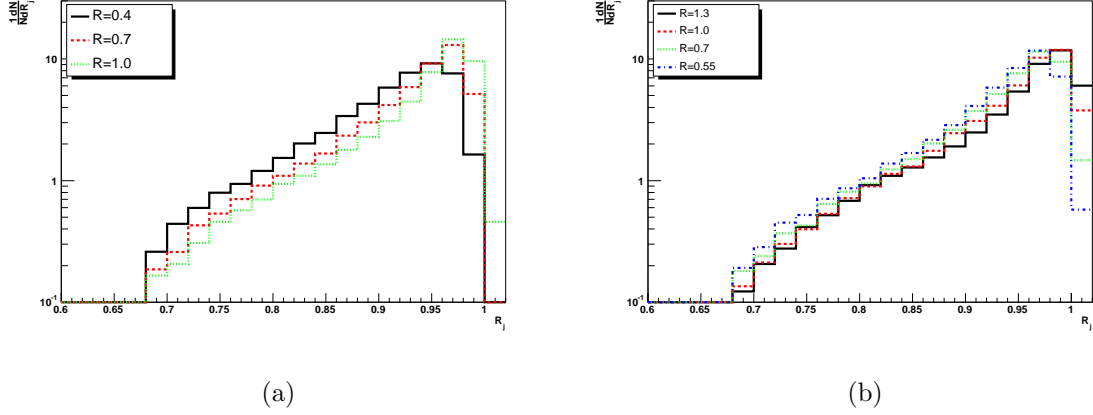


Figure 3.3: The reconstructed R_j distribution using the cone (a) and inclusive K_T (b) jet-finding algorithms. The R_j distribution is not as effected as R_{jj} when the cone radius or K_T R Parameter is changed.

The final kinematic matching variable is Δy shown in figure 3.4. Again, the K_T algorithm is less susceptible to changes in R_{K_T} . Both distributions have the majority of events concentrated in the region $\Delta y < 0.1$. The upshot of all this is that the R_j and Δy variables are extremely good at defining the exclusive event. Furthermore, it is possible to choose small values of R_{cone} or R_{K_T} without too much change in the reconstructed signal. This will be important in high luminosity running at the LHC with multiple pile-up events. Smaller values of R_{cone} and R_{K_T} will result in less particles from these overlap events being wrongly added into the events of interest.

The objective now is to define a set of exclusivity cuts which keeps as much of the signal as possible, whilst rejecting a large fraction of the background. The R_{jj} , R_j and Δy distributions for the central exclusive Higgs is plotted in figure 3.5 against the $b\bar{b}$ background produced via double pomeron exchange. A cone radius of 0.4 and a K_T R-parameter of 0.55 was used. The distributions are normalised

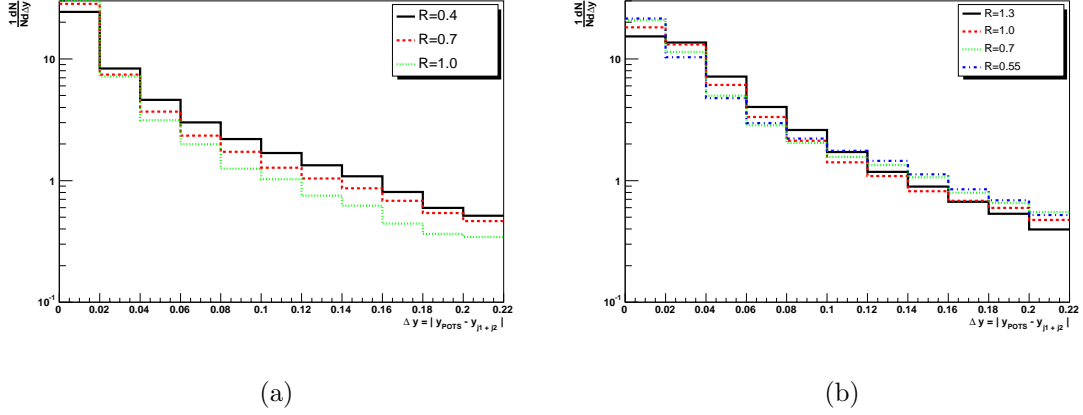
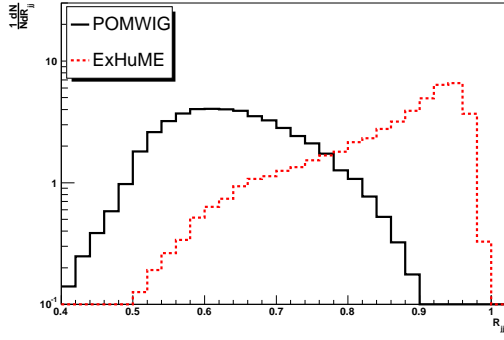


Figure 3.4: The reconstructed Δy distribution using the cone (a) and inclusive K_T (b) jet-finding algorithms.

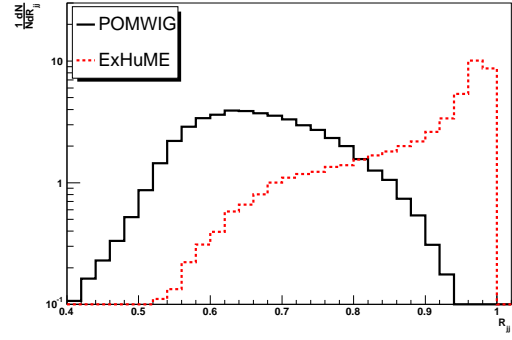
to 1.0 to show the general shape of the two different distributions. It should be noted that at this stage the double pomeron $b\bar{b}$ background is approximately 380 times larger in cross section than the signal although spread over a larger mass range.

The values $R_{cone} = 0.4$ and $R_{K_T} = 0.55$ are chosen for two reasons. Firstly they produce similar distributions and do not give a false impression that one algorithm is superior. Secondly, smaller values of R_{cone} and R_{K_T} are less likely to reconstruct di-jets containing some of the pomeron remnants. This is desirable as we are wanting to reconstruct the hard-scattering part of the double pomeron exchange process.

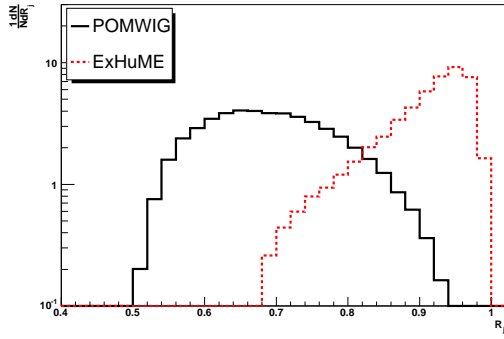
Using R_j instead of R_{jj} has some interesting effects. Firstly, as expected, the low R_{jj} tail is not present in the R_j distribution for both the signal and background. This initially leads us to presume that the R_j variable is better at reconstructing the mass of the hard-scatter than R_{jj} . However, for the double pomeron $b\bar{b}$ events, the R_j distribution extends to larger values than R_{jj} . Some of this increase can



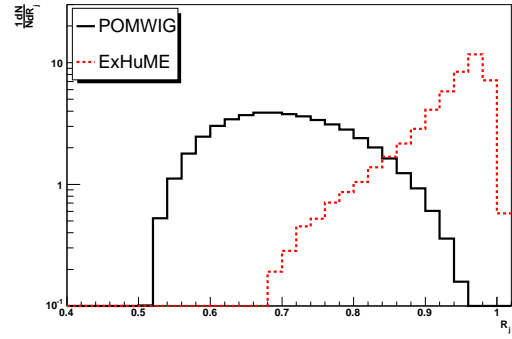
(a)



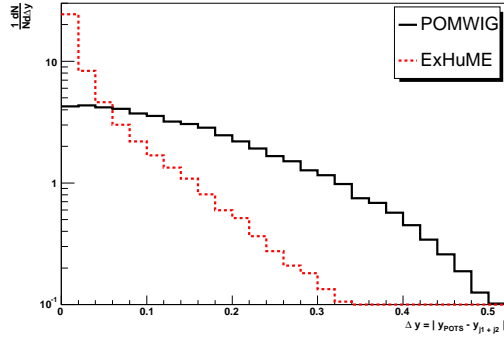
(b)



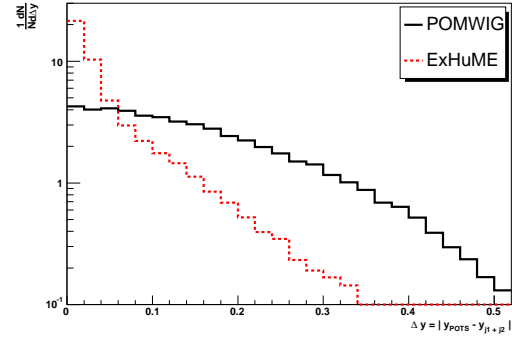
(c)



(d)



(e)



(f)

Figure 3.5: The normalised R_{jj} , R_j and Δy distributions for exclusive Higgs and double pomeron $b\bar{b}$ production using a cone radius of 0.4 (a, c, e) and inclusive K_T R-parameter of 0.55 (b, d, e).

be attributed to the highest E_T jet having a bit of pomeron remnant in it. This extra energy is then counted twice in the R_j reconstruction. This problem is reduced by the use of small values of R_{cone} and R_{K_T} but can never be completely removed. The second effect of using the R_j variable is that there seems to be a sharper, more distinct, separation between the signal and background. This is mainly due to the removal of the long tail of the signal in the R_j distribution. The Δy distribution is also well reconstructed. Smaller values of R_{cone} or R_{K_T} lead to a broader distribution with a long tail to large values of Δy . This is because hard radiation in the parton showering phase would lead to a significant change in direction of one of the jets if the energy from the radiation is reconstructed as a third jet.

The distributions presented in 3.5 give us a feel for the loosest possible cuts in those distributions. The loose cut is defined as the point at which the normalised signal and background distributions cross over. For example, a cut of $R_j > 0.85$ can be applied to di-jets reconstructed using the inclusive K_T algorithm with $R_{K_T} = 0.55$. Shifting this cut to the left will include a larger fraction of background with only a very small gain in signal. This loose cut is not the optimum cut for the analysis because the background is so much larger than the signal; it only tells us the region of interest for further study. The best cut will be found by later by requiring the best possible signal to all background ratio.

The cut value depends on the values of R_{cone} or R_{K_T} used to reconstruct the di-jets. Figure 3.6 shows how the cut values of R_{jj} and R_j change with the jet algorithm parameter. Using the K_T algorithm as an instructive example, it is clear that the R_j cut is less dependent on R_{K_T} than the R_{jj} cut - which changes less than 0.02 over the range of R_{K_T} used. The steep dependence of the R_{jj} cut

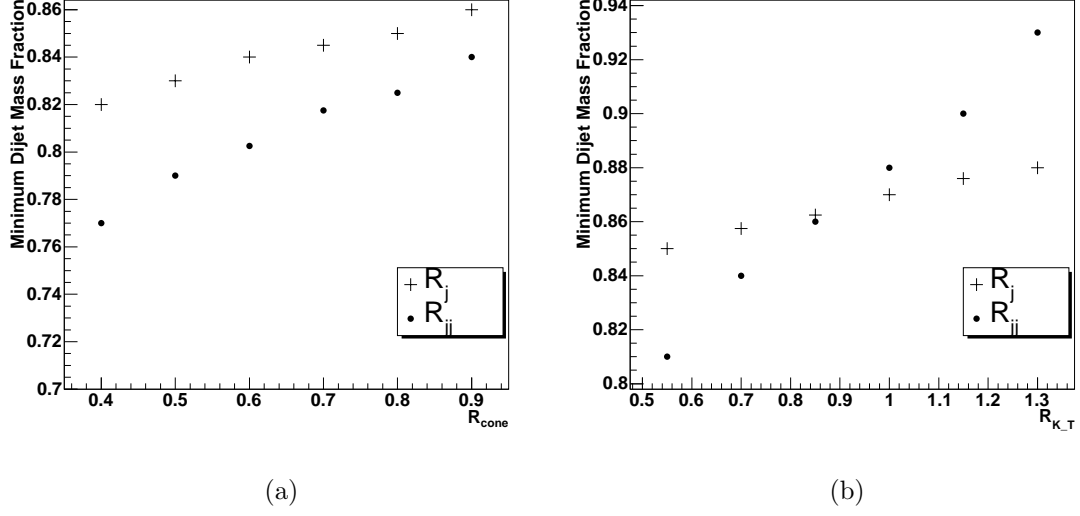


Figure 3.6: The dependence of the R_{jj} and R_j cuts as a function of R_{cone} (a) and R_{KT} (b).

with R_{KT} is easily understood because the signal is reconstructed with larger R_{jj} when R_{KT} is increased. Furthermore, the background will also be reconstructed with larger R_{jj} as it is just as susceptible to parton showering. Therefore the cut naturally increases to keep the signal efficiency high and the background efficiency low. A similar effect is found for the cone algorithm, but the dependence is less steep with R_{cone} .

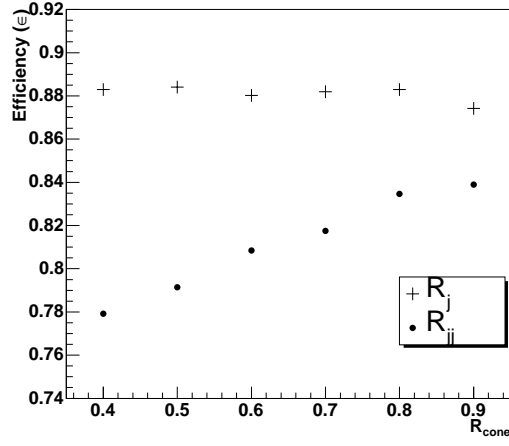
The R_j^{cut} however, is almost entirely dependent on the background reconstruction. Figure 3.3 showed that the reconstructed signal is almost R_{KT} independent. If the background followed the same trend then one would expect no R_{KT} dependence. The weak dependence arises because of the pomeron remnants. Again large values of R_{KT} are more likely to pull in some of the remnants, thus the cut increases to keep the background efficiency low. The performance of the cone algorithm is similar for the range of R_{cone} used.

The Δ_y^{cut} is always less than 0.1 and decreases as R_{K_T} increases due to there being less chance of the radiation escaping and changing the direction of the second jet. The cut on Δy is not examined further because this cut is lower than the granularity of the towers in the hadronic calorimeter. It is not certain that the direction of a jet can be measured more accurately than the tower granularity, therefore the exclusivity cut is set at $\Delta y < 0.1$ for the rest of the analysis.

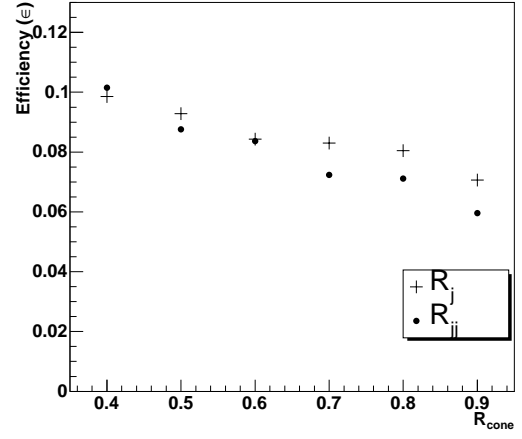
The reconstructed signal and background efficiencies as a function of R_{cone} and R_{K_T} is shown in figure 3.7. For each jet algorithm parameter, the preferred cuts given in figure 3.6 are used. For the signal, the performance of the cone and K_T algorithms are very similar. For R_j , the signal efficiency is virtually independent of both R_{cone} and R_{K_T} being flat at about 87%. For R_{jj} , the efficiency of the signal increases with R_{cone} and R_{K_T} . In all cases, the signal efficiency is always better for loose cuts on R_j than R_{jj} .

The reconstructed double pomeron background is more interesting. For the cone algorithm, the background efficiency is similar for cuts on R_j and R_{jj} and decreases with cone radius. The K_T algorithm on the other hand shows completely different dependence on R_{K_T} depending on whether R_{jj} or R_j is used. The background efficiency decreases with R_{K_T} if a cut on R_{jj} is made. However, smaller values of R_{K_T} are preferred if a cut on R_j is made.

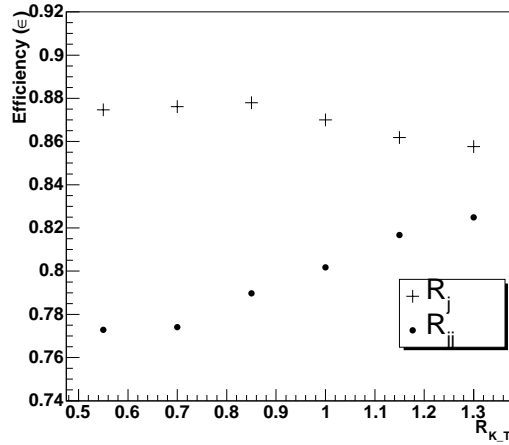
With all of the information on jet algorithm and kinematic matching variables investigated it is now possible to choose the best jet algorithm and basic kinematic matching cuts and then continue with the analysis. It is not a good idea however to simply pick the best signal to background performance, one must take into account the environment of ATLAS and the LHC. An example of this is the Δy^{cut} which could not be set below 0.1 because of the granularity of the hadron calorimeter.



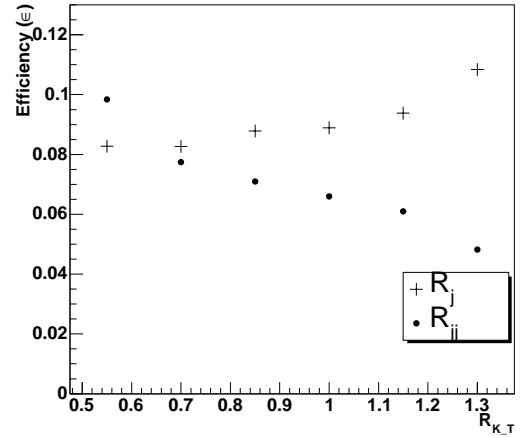
(a)



(b)



(c)



(d)

Figure 3.7: The dependence of the R_{jj} and R_j cuts as a function of R_{cone} (a, b) and R_{K_T} (c, d).

The resolution of the ATLAS detector could play a big part in rejecting some cuts. In [], the reconstructed jet σ_{E_T}/E_T was found to be approximately 5 – 8% depending on pseudo-rapidity and jet algorithm parameter. The resolution of the R_j variable will be dominated by this E_T resolution because FP420 has typically small values of σ_x/x . This means that R_j variable should not be constrained by a window smaller than $0.92 < R_j < 1.08$ and the R_{jj} window will be larger as it depends on the measurement of two transverse energies. In addition to detector effects, particles from pile-up events at the LHC can be wrongly reconstructed in the di-jet system. This problem can never be removed completely, but the best way to avoid pulling particles into jets is to use smaller R_{cone} or R_{K_T} .

Taking all factors into account, the following choices are made:

1. The jet algorithm parameters $R_{cone} = 0.4$ and $R_{K_T} = 0.55$ are chosen for the rest of the analysis. These small values are chosen to minimise the effect of pile-up and reduce the amount of pomeron remnant reconstructed in the dijet sample.
2. The small jet finding parameters result in the loose exclusivity cuts being defined as $0.82 < R_j < 1.15$ for the cone algorithm and $0.85 < R_j < 1.15$ for the K_T algorithm. The $\Delta y < 0.1$ cut is imposed for both algorithm choices.

No cuts are made at this point on R_{jj} .

Although these choices lead to a higher percentage of DPE passing the cuts, the signal efficiency is unaffected. Furthermore, the R_j cuts can be tightened later to reduce the background if necessary.

3.3.3 Simulation of the Overlap Background

The pile-up background cross section, σ_{pile} , can be estimated by

$$\sigma_{pile} = 0.5N(N-1)P_i^2Q\sigma_{QCD} \quad (3.5)$$

where N is the number of pile-up events per bunch crossing, P_i is the probability of an event at the LHC being a single diffractive event which will cause a hit in FP420 and Q is the QUARTIC rejection factor. The input cross section, σ_{QCD} , is the cross section of normal inclusive events ($b\bar{b}$ or light jets, jj) generated by the HERWIG event generator [?].

The number of pile-up events at the LHC depends upon the luminosity and is considered to be a linear relationship. The QUARTIC rejection factor is calculated by picking three random vertices according to a gaussian distribution of width 5.6cm about the $z=0$ point. The 5.6cm is the longitudinal beam spot size at the LHC. Two of these vertices correspond to the SD events and the average corresponds to the fake vertex measured by QUARTIC. If the final vertex, which corresponds to the primary QCD event, is within 2.1mm of the fake vertex then the event will pass the QUARTIC measurement. It is found that only 2.5% of overlap events will pass this requirement. This is in good agreement with [?]. P_i is estimated by

$$P_i = \frac{\sigma_{SD}\epsilon_{SD}}{\sigma_{TOT}} \quad (3.6)$$

where σ_{TOT} and σ_{SD} are the total and single diffractive cross sections at the LHC obtained from the PYTHIA event generator [?]. The protons from the SD events are then passed to the FPTRACK program [?] to obtain, ϵ_{SD} , the percentage of single diffractive events that produce a hit in FP420. The result is $P_i = 0.012$.

The total pile-up cross section can then be reduced by kinematic matching. The overlap background events are constructed in two steps. The QCD event is

generated using the HERWIG Monte Carlo. The protons are then constructed using Monte Carlo methods. The pomeron flux factor given in section ?? is an analytic function in both x and t . The values of x and t are then distributed between $[x_{min}, x_{max}]$ and $[t_{min}, t_{max}]$ (determined by the acceptance of FP420) using the techniques presented in section ?? to give the correct distributions.

3.3.4 Results

It is now possible to estimate the signal to background ratio for this analysis. The following cuts are then made on the MC samples:

1. The K_T jet algorithm is used with $R_{K_T} = 0.55$.
2. The highest transverse energy jet must satisfy $E_T > 40 GeV$
3. The longitudinal momentum loss of each proton must lie in the range $0.002 < x_i < 0.015$.
4. The di-jet mass fraction must be in the range $0.85 < R_j < 1.15$.
5. $\Delta y < 0.1$.

The first requirement is the choice of jet finding algorithm discussed in section. Cut 3 limits the protons to hit the pots at 420m. The final 2 cuts are the reduction of background by kinematic matching as discussed in section 3.3.2. The input cross sections, defined as cuts 1-3 in the list above, are shown in table 3.1. The large gg and jj backgrounds are reduced by b-tagging. The ATLAS detector is capable of identifying b jets with an efficiency of 0.6 but with a mis-tag of just 0.01. Thus the cross sections presented in table 3.1 have to be multiplied by 0.36 or 10^{-4} (depending on the process involved) to reflect this.

Generator	Process	Cross section (fb)
ExHuME	$H \rightarrow b\bar{b}$	
	$b\bar{b}$	
	gg	
POMWIG	$b\bar{b}$	
	jj	
HERWIG + SD	$b\bar{b}$	
	jj	

Table 3.1: The input cross sections for signal and background. All samples have had a $E_T > 40$ GeV cut applied to the highest transverse energy jet after jet finding with the K_T algorithm with an R parameter of 0.55. The proton momentum loss have also been restricted to the range 0.002 - 0.015.

The backgrounds can be reduced by cutting a mass window around the Higgs peak. The mass resolution of FP420 is taken to be $\sigma_{M_X} = 0.01M_X$ which is a sensible estimate of the FP420 mass resolution given in section ???. The mass distributions for the signal and background are shown in figure 3.8 after smearing the value of M_X by a gaussian of width $0.01M_X$. The backgrounds are all continuous across the region of interest, thus a mass window of 2GeV either side of the Higgs peak is applied to the sample. The R_j distribution, after the cut on the mass measured in the pots, is shown in figure 3.8. It is clear that the R_j window will have to be tightened to remove more background.

The overlap background can be reduced further by cutting on the number of charged tracks outside the two main jets. The ATLAS inner detector can measure the track vertex to an accuracy of $< 500\mu\text{m}$. An exclusive event will only have tracks originating from the $b\bar{b}$ associated with the vertex. The overlap events

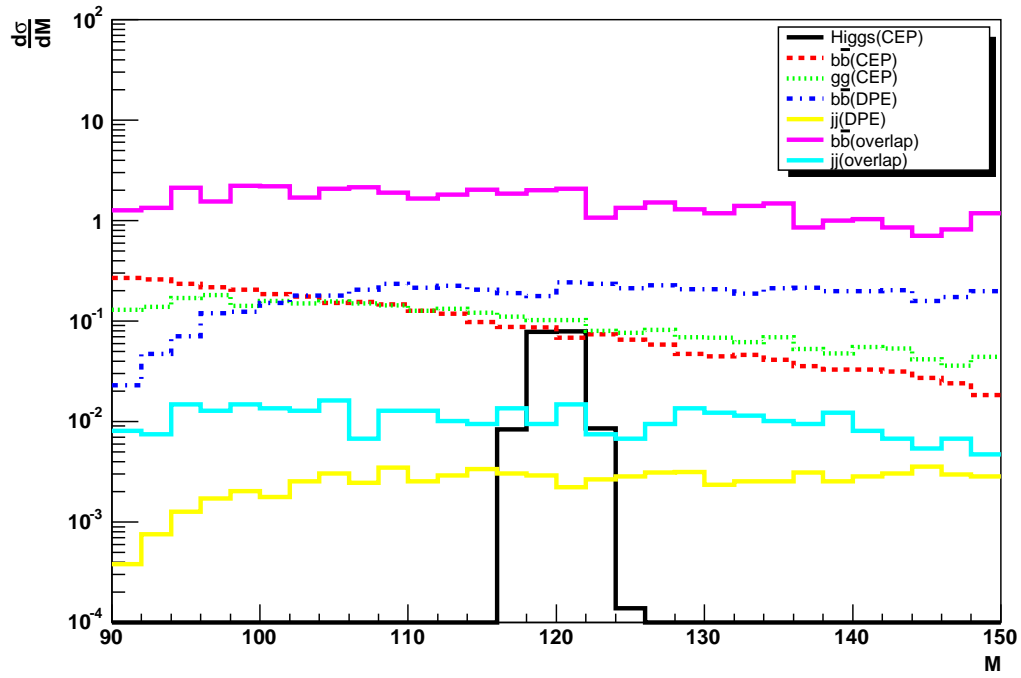


Figure 3.8: The mass distributions of signal and background events as measured by FP420 (a). The mass, M_X , has been smeared by a gaussian of width $0.01M_X$ to approximate the resolution of FP420.

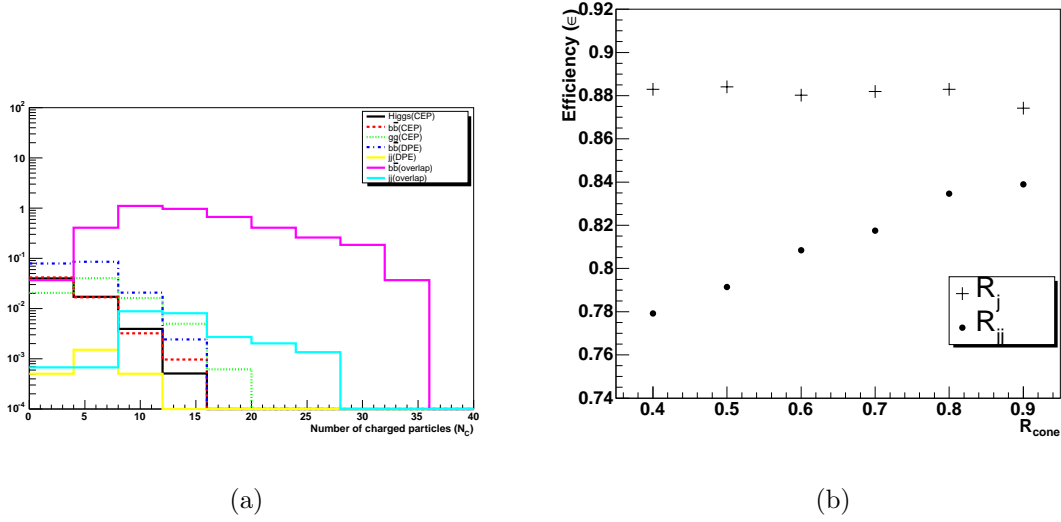


Figure 3.9: The number of charge tracks (a) associated with the primary vertex that have $p_T > 0.5 GeV$ and lie in the range $|\eta| < 2.5$. Also shown (b) is the probability of pile-up events being close enough to the primary vertex to ruin the cut on the number of charged tracks outside the two main jets.

however have an inclusive QCD event as the primary vertex. This means that there will be particles from the break up of the protons themselves. If these particles are charged and lie within the pseudo-rapidity coverage of the inner detector, it will be possible to make a cut on them. The number of charged tracks in the pseudo-rapidity range $|\eta| < 2.5$ with a $p_T > 0.5 GeV$ is shown in figure ??.

Clearly the distribution of charged tracks is different for the events in which the protons remain intact, making this variable a good discriminator for all diffractive events, not just exclusive ones. The usefulness of this variable however will be limited at higher luminosities where the probability of a pile-up event being close to the primary vertex will be larger as the number of pile-up events per bunch crossing increases.

The probability of a pile-up event being within $500\mu\text{m}$ of the primary event can be estimated as a function of luminosity in the same way that the QUARTIC rejection factor was estimated in section 3.3.3. Firstly, N vertices are created to mimic the number of pile-up events at the LHC at a particular luminosity. The first vertex represents the primary vertex and the others the pile-up events. If any of the pile-up events are within $500\mu\text{m}$ of the primary vertex, then the event would have to be thrown away. The probability of an event being removed in this way is shown in figure ??.

3.3.5 Trigger Consideration